Deformation and fracture under compressive loading in lamellar TiAl microstructures

By MING DAO, BIMAL K. KAD and ROBERT J. ASARO

Department of Applied Mechanics and Engineering Sciences, University of
California-San Diego, La Jolla, California 92093-0411, USA

ABSTRACT

A physically based micromechanical model is applied to study finite
compressive deformation behaviour and the development of failure modes in
polycrystalline fully lamellar and nearly lamellar microstructures. Orientation-
dependent yielding of lamellar TiAl single crystals is specifically modelled.
Finite-element computations show that deformation is inherently non-uniform
in the lamellar microstructure, in accordance with results presented earlier by
Kad, Dao and Asaro. Intergranular fracture initiation is found to be expected
at small aggregate strains (i.e. strains less than 5%), while fracture initiated by
internal buckling is found to be increasingly likely to occur at larger aggregate
strains (i.e. strains larger than 5–10%). Internal buckling is found in lamellar TiAl
crystals whose lamellae are initially nearly parallel to the compressive loading. A
weak basal texture, normal to the compression axis, is developed at only 20%
aggregate strain. Subtle variations in microstructural constituents in lamellar and
nearly lamellar TiAl are found to have significant influences on the flow and
fracture behaviour.

§ 1. INTRODUCTION

Two-phase γ-TiAl $(L1_0)$ + α_2-Ti$_3$Al$(D0_{19})$ alloys with fine scale (about 1–2 μm)
lamellar microstructures demonstrate improved ductilities and fracture toughness
over their monolithic constituents. The research on lamellar and nearly lamellar
(NL) TiAl has received extensive attention in the last 15 years (see Kim (1991) for
a recent review). In a recent study by Kad, Dao and Asaro (1995a), deformation
under tension was found to be extremely inhomogeneous, resulting in a strong
concentration of tensile hydrostatic stresses at the grain boundaries which thereby
promoted intergranular fracture initiation. In particular, the increase in ductility in
polycrystalline microstructures with increasing equiaxed γ-grain volume fraction
(with compliant deformation characteristics) in NL alloys is explained by the reduc-
tion in the hydrostatic stress build-up near the boundaries, consequently mitigating
fracture.

While tensile properties are important, primarily from an *in-service* design per-
spective, compressive mechanical behaviour is also very important, particularly in
deformation processing used to create large shape changes. A comprehensive under-
standing of deformation and fracture under compressive loading in lamellar TiAl
microstructures is crucial in determining the mechanical workability.

To model lamellar TiAl microstructures, it is very important to account for the
orientation dependence of the yield strength. In the laminate form, γ-TiAl is the
softer phase and a flow anisotropy is derived particularly from the laminate geome-

try such that shear deformtion parallel to the slabs (soft mode) is easier than across the slabs (hard mode) owing to the difficulty of propagating slip through the harder α_2-phase (Fujiwara *et al.* 1990). The yield strength of lamellar single crystals is, accordingly, orientation dependent (figure 1) (Inui, Oh, Nakamura and Yamaguchi 1992). In an analogous manner, single colonies also exhibit orientation-dependent fracture strains (fig. 1). In addition, fatigue crack growth exhibits a rate anisotropy of 2.7×10^{-7} m/cycle as against 7×10^{-7} m/cycle respectively for growth perpendicular and parallel to the laminates (Davidson and Campbell 1993). The highly orientation-dependent microstructure in lamellar TiAl single crystals may induce internal buckling within the polycrystalline microstructure at large compressive strains (i.e. strains larger than 5%). As an example, Chan and Kim (1993) reported buckling in a nearly lamellar sample deformed to about 24% strain at 800°C.

The other important aspect of the deformation of polycrystalline lamellar TiAl microstructures is that the deformation is inherently non-uniform. Therefore classical Taylor type of models cannot accurately account for the details of the deformation and localization development, where deformation within one crystal is assumed to be uniform. Harren and Asaro (1989) employed finite-element techniques for ductile fcc or bcc polycrystals, to account rigorously for these effects and revealed that non-uniform deformations, and strain localizations naturally arise in polycrystals as a consequence of the crystallographic slip process. Further, these finite-element calculations provide insight into identifying the mechanisms that contribute to localized deformation effects. Since localized regions are prevalent in large strain deformations, they must affect, to some degree, the global stress–strain response and mechanical behaviour in general. With limited slip systems available (i.e. fewer than five independent slip systems to satisfy the von Mises criteria of macroscopic plasticity) and a large difference in critical resolved shear stress (CRSS) between the soft-mode and hard-mode slip systems, localized deformation is expected to begin at small strains, and large hydrostatic stresses may develop across neighbouring crystals owing to the associated strain incompatibilities.

In extending our previous work (Kad, Dao and Asaro 1995a, b, c, Dao, Kad and Asaro 1995), the objective of this study is twofold: first to understand the deformation and failure mechanisms in polycrystalline lamellar TiAl microstructures under large strain compressive loading (i.e. aggregate strains larger than 5%) and, secondly, to study the microstructural subtleties and their influence towards the com-

Fig. 1
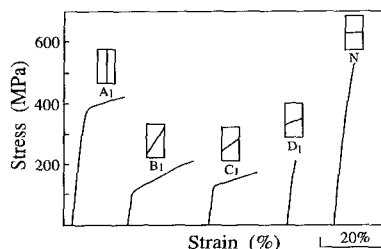
Orientation dependent stress–strain behaviour in single crystals of lamellar TiAl. (Reproduced from Inui *et al.* (1992).)

pressive mechanical properties. The results are directly useful in defining the best microstructural design.

The plan of the paper is as follows. The constitutive theory and microstructural modelling are described in §2. In §§3.1–3.4, results are presented in terms of stress–strain behaviour, localized deformation, lattice rotations and texture development, and internal failure modes, and in §3.5 a discussion on the influence of the intermediate mode is made. Finally, conclusions are given in §4.

§ 2. THEORETICAL AND MICROSTRUCTURAL CONSIDERATIONS

Standard tensor notation is used throughout the following development. Bold symbols are used to denote vectors and high-order tensors, the order of which will be clear in context. Products are indicated with dots, which denote summation over repeated Latin indices, and products containing no dots are dyadic products. Latin indices range from one to the number of spatial dimensions, and repeated Latin indices are always summed. Inverses, transposes, and transposed inverses are denoted with a superscript -1, T and $-$T, respectively and superposed dots indicate differentiation with respect to time t. For example,

$$\mathbf{A \cdot B} = A_{ik}B_{kj}\mathbf{b}_i\mathbf{b}_j, \quad \mathbf{A \times B} = e_{ijk}A_jB_k\mathbf{b}_i,$$

$$\mathbf{A : B} = A_{ij}B_{ji}, \quad \mathbf{AB} = A_{ij}B_{kl}\mathbf{b}_i\mathbf{b}_j\mathbf{b}_k\mathbf{b}_l,$$

$$\mathbf{cd} = c_id_j\mathbf{b}_i\mathbf{b}_j, \quad \mathbf{B \cdot c} = B_{ij}c_j\mathbf{b}_i,$$

$$\frac{\partial \mathbf{c}}{\partial \mathbf{d}} = \frac{\partial c_i}{\partial d_j}\mathbf{b}_i\mathbf{b}_j, \quad \dot{\mathbf{B}} = \frac{\partial B_{ij}}{\partial t}\mathbf{b}_i\mathbf{b}_j,$$

$$\mathbf{H : A} = H_{ijkl}A_{lk}\mathbf{b}_i\mathbf{b}_j,$$

where e_{ijk} is the permutation symbol. The basis $\mathbf{b}_i$ is Cartesian and independent of time. Greek indices are used to identify slip systems and range from one to N, the number of slip systems. Summation over repeated non-parenthetical Greek indices is implied while repeated parenthetical Greek indices are not summed, for example $\mathbf{c}_\alpha\mathbf{d}_\alpha$ means $\mathbf{c}_1\mathbf{d}_1 + \mathbf{c}_2\mathbf{d}_2 + \ldots + \mathbf{c}_N\mathbf{d}_N$ and $\mathbf{c}_\alpha\mathbf{d}_{(\alpha)}$ means either $\mathbf{c}_1\mathbf{d}_1, \mathbf{c}_2\mathbf{d}_2, \ldots$ or $\mathbf{c}_N\mathbf{d}_N$.

2.1. *Constitutive theory*

The theoretical description in the ordered alloys used in the analyses to be described and proposed is based on a strain-rate and temperature dependent description of crystalline slip. The theory, in its present form, was developed by Asaro and Rice (1977), Asaro (1979), Pierce, Asaro and Needleman (1983), Harren, Dève and Asaro (1988), McHugh, Asaro and Shih (1993) and, most recently Dao and Asaro (1993). It is based on the earlier work of Hill (1962) and Hill and Rice (1972). Our theory accounts for arbitrarily large deformations and rotations of *both* the material *and* the underlying crystalline lattice. Texture development and the resulting anisotropic material response are thereby accounted for together with a wide array of localized modes of deformation that are specifically important in the overall deformation behaviour of TiAl lamellar microstructures as well as in the development of failure. As described below, this theory has been implemented in finite-element codes to perform particular analyses of microstructural response as well as to conduct

thermomechanical process modelling. Such analyses are particularly important for intermetallic alloys, which inherently are of low symmetry, and specifically for TiAl alloys with oriented lamellar microstructures which further reduce symmetry.

The total deformation gradient $\mathbf{F}$ is decomposed into plastic ($\mathbf{F}^P$), thermal ($\mathbf{F}^\theta$), and lattice ($\mathbf{F}^*$) parts; that is, if $\mathbf{u}$ is the displacement vector and $\mathbf{X}$ the material position vector with respect to the reference (undeformed) state, then $\mathbf{F} = \mathbf{I} + \partial\mathbf{u}/\partial\mathbf{X}$ ($\mathbf{I}$ is the second-order identity tensor), and

$$\mathbf{F} = \mathbf{F}^* \cdot \mathbf{F}^\theta \cdot \mathbf{F}^P. \tag{1}$$

Plastic deformation occurs by the flow of material through the lattice, via simple shearing, across planes with unit normals $\mathbf{m}_\alpha$ and in directions $\mathbf{s}_\alpha$; here $\mathbf{m}_\alpha$ and $\mathbf{s}_\alpha$ represent a crystallographic slip plane normal and a slip direction respectively and α is an index that designates a slip system. If $\dot{\gamma}_\alpha$ is the slip rate on the α slip system, then

$$\dot{\mathbf{F}}^P \cdot (\mathbf{F}^P)^{-1} = \dot{\gamma}_\alpha \mathbf{s}_\alpha \mathbf{m}_{(\alpha)}, \tag{2}$$

where the summation is over all active slip systems.

From this plastically sheared state, thermal deformation occurs owing to temperature changes. If $\boldsymbol{\alpha}(= \alpha_{ij}\mathbf{a}_i\mathbf{a}_j)$ is a tensor of thermal expansion (α_{ij} are the coefficients of thermal expansion referenced to lattice vectors $\mathbf{a}_i$), then

$$\dot{\mathbf{F}}^\theta \cdot (\mathbf{F}^\theta)^{-1} = \dot{\theta}\boldsymbol{\alpha}, \tag{3}$$

where $\dot{\theta}$ is the rate of temperature change.

In general $\dot{\gamma}_\alpha$ will be a function of temperature, stress state and material state. As a specific example we have used expressions such as

$$\dot{\gamma}_\alpha = \dot{a}\,\mathrm{sgn}\,\{\tau_\alpha\}\left\{\left|\frac{\tau_{(\alpha)}^D}{g_{(\alpha)}}\right|\right\}^{1/m} \tag{4}$$

to represent strain-rate-sensitive power-law-type behaviour. τ_α is the resolved shear stress on slip system α, $g_\alpha > 0$ is its current strength, and τ_α^D is the *loading parameter* that may be written as

$$\tau_\alpha^D = \tau_\alpha + \boldsymbol{\eta}_\alpha : \boldsymbol{\tau}, \tag{5}$$

where $\boldsymbol{\tau}$ is the Kirchhoff stress tensor and $\boldsymbol{\eta}_\alpha$ is the tensor of *non-Schmid effects* originally introduced by Asaro and Rice (1977) and recently extended within an elasto-plastic rate-dependent multiple-slip framework by Dao and Asaro (1993). Even common metals display departures from the Schmid rule and these have, as shown originally by Asaro and Rice (1977), the effect of destabilizing uniform plastic flow.

The slip system hardness g_α is obtained by path-dependent integration of the evolution equations of the form

$$\dot{g}_\alpha = \sum_\beta h_{\alpha\beta}(\gamma_a)|\dot{\gamma}_\beta| + g_\alpha^\theta\dot{\theta}, \quad \gamma_\alpha = \int_0^t \sum_\alpha |\dot{\gamma}_\alpha|\,\mathrm{d}t \tag{6}$$

where $h_{\alpha\beta}$ is a matrix of hardening moduli and g_α^θ is the rate of change in slip system hardness with respect to temperature alone. The initial condition for this evolution is given by $g_\alpha(\gamma_a = 0, \theta = \theta_0) = g_\alpha(\theta_0) = g_\alpha^0$, where θ_0 is an initial temperature. As

eqn. (6) indicates, both slip systems *self-hardening* as well as coupled (i.e. *latent*) hardening are accounted for, together with thermal softening.

The detailed development of the constitutive relations can be found in the paper by Dao and Asaro (1993), This very general constitutive theory has been implemented into finite-element codes, using the rate tangent method introduced by Pierce *et al.* (1983). Although the model has the ability to deal with more complex problems including temperature variation and/or non-Schmid effects, the present problem deals with only isothermal deformations without any non-Schmid effects. Thus explicit references to temperature and non-Schmid terms are neglected henceforth.

2.2. *Microstructural considerations*

Complete, three-dimensional finite-element polycrystal analyses require large amounts of computer memory and central processing unit time. For this reason, such analyses are done sparingly. Fortunately much progress can be made using two-dimensional models to study the deformation and failure modes in TiAl polycrystals. The idealization used here was motivated by the previous two-dimensional polycrystal models of Harren *et al.* (1988), Harren and Asaro (1989) and McHugh *et al.* (1993) originally intended for fcc or bcc polycrystals and their metal matrix composites. The specific particulars for lamellar TiAl are described below.

2.2.1. *Two-dimensional modelling of polysynthetically twinned (PST) single crystals*

The essential prerequisite to modelling the anisotropic deformation (fig.1) is to include the essential microscopic anisotropies of the slip and/or twinning deformation modes of the constituent phases into the aggregate theory. The slip systems in order of increasing CRSS in α_2-Ti$_3$Al phase are firstly the $\langle 11\bar{2}0\rangle\{10\bar{1}0\}$ prism slip system (about 100 MPa), secondly the $\langle 11\bar{2}0\rangle(0001)$ basal slip system (about 330 MPa), and thirdly the $\langle 11\bar{2}6\rangle\{11\bar{2}1\}$ pyramidal slip system (about 910 MPa). The slip systems in the γ-TiAl phase, in order of increasing CRSS are firstly the $\langle 1\bar{1}0]\{111\}$ perfect dislocation slip system, secondly the $\langle 011]\{111\}$, and thirdly the $\langle 112]\{111\}$ superdislocation slip systems. In lamellar alloys, three different deformation modes are possible.

(1) *The soft mode* is lamellar oriented at about 45° to the loading axis. Deformation occurs in the soft γ-phase with deformation vectors parallel to the lamellar interface. No constraints are exerted by the α_2-phase. Soft mode resistance is affected by colony or domain size.

(2) *The intermediate mode* is lamellar oriented paralled (about 0°) to the loading axis. Deformation occurs in the soft γ-phase with deformation vectors parallel to the lamellar interface, but gliding on the cross-slip planes. In this configuration, the maximum constraint exerted by the α_2-phase is determined by the stress required to activate $\langle 11\bar{2}0\rangle\{10\bar{1}0\}$ prism slip which is nearly equal to 100 MPa. Intermediate-mode resistance is affected by colony or domain size.

(3) *The hard mode* is lamellar oriented perpendicular (about 90°) to the loading axis. Maximum constraint exerted by the α_2-phase is determined by the stress required to activate the $\langle 11\bar{2}6\rangle\{11\bar{2}1\}$ pyramidal slip, about 910 MPa. This constraint is, however, strongly scale dependent (i.e. lamellar thickness).

Certain simplifying and valid assumptions are made to reduce the three-dimensional slip system input for the two-dimensional plane-strain simulations described here. In the two-dimensional model, the ascribed slip system geometry (see fig. 2), is based on the composite $\gamma + \alpha_2$ mixture. Thus the soft mode ($\mathbf{s}_1$, $\mathbf{m}_1$) is ascribed to the γ-TiAl phase; the hard modes ($\mathbf{s}_2$, $\mathbf{m}_2$) and ($\mathbf{s}_3$, $\mathbf{m}_3$) are ascribed to the α_2-Ti$_3$Al phase.

In the examples described here, the input employs only two unique slip systems (i.e. the soft mode and the hard mode) in an isosceles triangle. In this two-dimensional configuration, the lamellar normals are configured to lie in plane, and only in-plane vectors are considered. Finally, in the specific example of lamellar TiAl, the model does not specify initial orientations about the lamellar normal, since the yield stress is essentially constant for any such rotations (Fujiwara *et al.* 1990).

Since the material response would depend largely on the plastic property of the crystals, we take the elasticity to be isotropic, where Lame's constant λ and the elastic shear modulus μ are used. The lattice is assumed to deform in plain strain. The hardening is a simple linear hardening, with no latent hardening. The hardening matrix $h_{\alpha\beta}$ in eqn. (6) is given as

$$h_{11} \text{ is the soft-mode hardening rate,}$$

$$h_{22} = h_{33} \text{ is the hard mode hardening rate,} \tag{7}$$

$$h_{ij} = 0 (i \neq j).$$

2.2.2. *Polycrystalline modelling*

The reference configuration of the two-dimensional single-crystal mode was shown earlier (see fig. 2 (*b*)). The three slip systems of the single crystal are arranged

Fig. 2

(*a*)   (*b*)   (*c*)
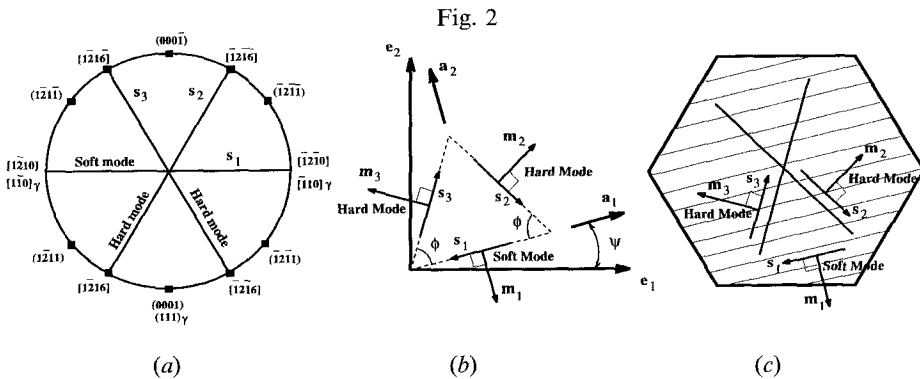
Two-dimensional schematic diagram of soft and hard-mode slip systems in the laminate morphology. (*a*) Projected two-dimensional slip systems; τ_{CRSS} (soft mode) $= g_1^0$ derived from shear in γ-TiAl parallel to the laminates and τ_{CRSS} (hard mode) $= g_2^0 = g_3^0$ derived from the $\langle 11\bar{2}6\rangle\{11\bar{2}1\}$ pyramidal slip system constraint imposed by the harder α_2-Ti$_3$Al phase. $\{\bar{1}010\}$ projection of α_2-Ti$_3$Al, incorporating the lamella normal in the plane of the sample for the two-dimensional approximation. Only in-plane Burgers vectors are considered in the two-dimensional model. (*b*) Final construction of the input slip-system morphology for the two-dimensional model. (*c*) Embedding the projected two-dimensional slip geometry into the single-crystal lamellar morphology.

in a triangle, and the reference crystal base vectors $\mathbf{a}_i$ are aligned with the crystal lattice as shown. Reference laboratory base vectors $\mathbf{e}_i$ are at an angle ψ with respect to reference crystal base vectors $\mathbf{a}_i$. In the $\alpha_2 + \gamma$ lamellar structure, the slip system $(\mathbf{s}_1, \mathbf{m}_1)$ is the soft-mode slip system; the slip systems $(\mathbf{s}_2, \mathbf{m}_2)$ and $(\mathbf{s}_3, \mathbf{m}_3)$ are equivalent hard-mode slip systems, where $\phi = 58°$. For duplex γ-TiAl single crystals, the slip systems $(\mathbf{s}_1, \mathbf{m}_1)$, $(\mathbf{s}_2, \mathbf{m}_2)$ and $(\mathbf{s}_3, \mathbf{m}_3)$ are taken as equivalent slip systems, where $\phi = 60°$.

The reference configuration of the two-dimensional polycrystal microstructure to be analysed is shown in fig. 3 (a), where the Cartesian base vectors $\mathbf{e}_i$ describe the orientation of the polycrystal's reference configuration with respect to the laboratory. Each of the 27 grains (or single PSTs) indicated in fig. 3 (a) is defined by an orthogonal transformation $\mathbf{a}_i^n = \psi_{ij}(\psi^n)\mathbf{e}_j$, $n = 1, \ldots 27$, where ψ^n is the angle ψ shown in fig. 2 (b) for the nth grain. Since a symmetry operation for each grain is a 180° rotation about the $\mathbf{e}_3$ axis, a random value between 0° and 180° was assigned to each grain with respect to $\mathbf{e}_3$. Without losing any generality, we take the angles to be integral degrees. Note that it would be straightforward to include pre-texturing with the model. In any event the aggregate will develop texture as a natural outcome of the deformation process.

The finite-element mesh used in the polycrystal calculations initially of rectangular 'crossed-triangle' quadrilateral elements in a uniform grid 40 rectangles wide by 56 rectangles high, which is 8960 constant-strain triangles totally (fig. 3 (b)). No geometric imperfections were present in the initial mesh. The mesh dimensions were chosen to represent equiaxed grains. Finally, all of the grain boundaries in this polycrystal model coincide with either an edge or a diagonal of a quadrilateral element, i.e. with an edge of a constant-strain triangle.

As stressed by Harren *et al.* (1988), the grain boundaries are 'continuum grain boundaries'. This is a continuum theory, and the polycrystal's initial reference configuration is assumed to be stress free and without any lattice perturbations. In fact each grain boundary is a line across which the initial lattice orientation ψ^n has a
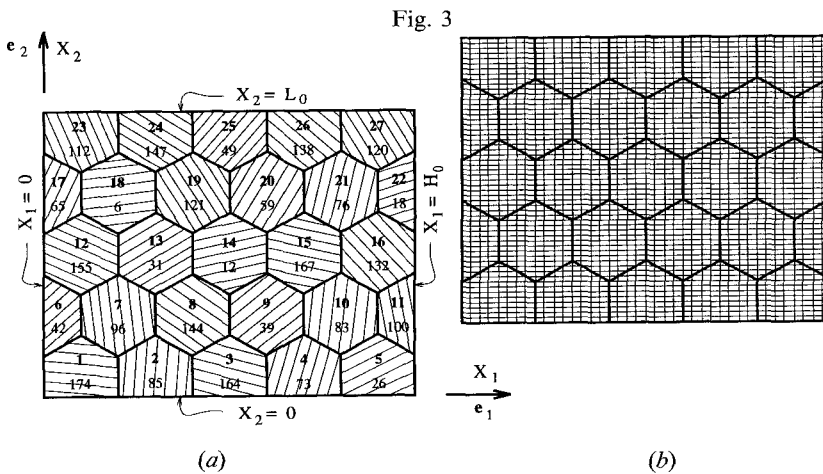
Fig. 3

(a) (b)

(a) Reference configuration of the 27 lamellar crystals representing the randomly generated polycrystalline aggregate. The orientations ψ^n shown are selected in the $0° \leqslant \psi^n < 180°$ range. (b) The initial finite element mesh.

jump.

The loading histories that are prescribed are constrained to be orthotropic, but, with respect to the polycrystal's reference configuration in fig. 3 (a), there is no special symmetry for this aggregate and one would not expect it to deform with orthotropic symmetry. Nevertheless, we take this aggregate as a material 'point' in a polycrystal material, and make a Taylor-like assumption that the deformation gradient of this aggregate (which is represented by the four straight lateral boundaries) is the same as the global deformation gradient. For the simple tension and compression simulations, the boundary conditions are

$$\dot{u}_2(X_1, 0) = 0, \ \dot{t}_1(X_1, 0) = 0,$$

$$\dot{u}_1(0, X_2) = 0, \ \dot{t}_2(0, X_2) = 0,$$

$$\dot{u}_1(H_0, X_2) = \dot{U}_1, \ \dot{t}_2(H_0, X_2) = 0, \qquad (8)$$

$$\dot{u}_2(X_1, L_0) = \dot{U}_2, \ \dot{t}_1(X_1, L_0) = 0.$$

Here, $\dot{\mathbf{u}} = \dot{u}_i \mathbf{e}_i$ is the material particle velocity, $\dot{\mathbf{t}} = \dot{t}_i \mathbf{e}_i$ is the rate of nominal traction, that is $\dot{\mathbf{t}} = \mathbf{N} \cdot \dot{\mathbf{n}}$ ($\mathbf{N}$ is the outward unit normal to the aggregate boundaries), $\dot{U}_1$ is the normal velocity on the material face $X_1 = H_0$ and $\dot{U}_2$ is the normal velocity on the material face $X_2 = L_0$. Also, the total loads on the unit cell (polycrystal aggregate) in X_1 and X_2 directions are respectively

$$P_1 = \int_0^{L_0} t_1(H_0, X_2) \, \mathrm{d}X_2, \ P_2 = \int_0^{H_0} t_2(X_1, L_0) \, \mathrm{d}X_1. \qquad (9)$$

The prescription for boundary value problem is completed by setting $\dot{P}_1 = 0$ and $\dot{U}_2/L_0 = \dot{a}$ for tension or $\dot{U}_2/L_0 = -\dot{a}$ for compression, and hence $\dot{U}_1$ and $\dot{P}_2$ are unknowns to be solved during the course of the solution of the rate boundary value problem. The initial state of this problem corresponds to zero stress and zero strain.

To account for a small to modest volume fraction of γ-TiAl phase, located at the grain boundaries due to the heat treatments, second-phase 'corner grains' were constructed, as illustrated in fig. 4. The corner morphology is designed with 4 or

Fig. 4

(a)   (b)   (c)
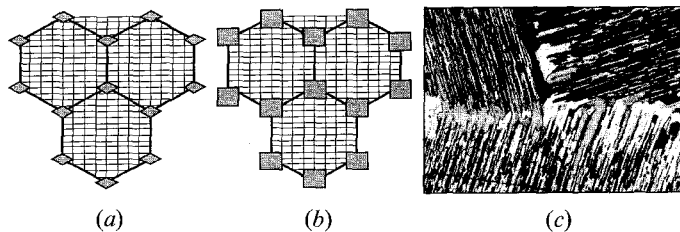
Construction of 'grain corners' of duplex γ-TiAl, as precipitated from the α-phase on heat treatment for NL microstructures; (a) 4 vol%, (b) 12 vol%, (c) actual microstructure of the lamellar geometry obtained by continuous cooling through the $\alpha + \gamma$-phase field. Specific detail of the microstructure in the vicinity of the triple point is of interest.

12 vol% second-phase 'corner grains'. For each of these γ-TiAl corner grains, ψ is assigned a random orientation angle $0° \leqslant \psi < 60°$.

2.2.3. *Input data for two-dimensional idealization*

As discussed by Kad *et al.* (1995a), Hall–Petch correlations provide a simple comparison between scale-independent modelling predictions and experimental observations. Thus, for any given microstructure, the soft mode is determined by the grain size (more appropriately the domain size) and the hard mode is determined by the individual thickness of slabs (cooling rate effect) and the volume fraction of α_2 (composition effect). The soft-mode CRSS is virtually independent of α_2 and shows little variation (maximum 50%) even for domain size effect. Thus the soft-mode CRSS may be in the range of 50–75 MPa, and the hard-mode CRSS may be in the range of 300–1200 MPa. After reviewing the existing experimental data (Inui *et al.* 1992, Fujiwara *et al.* 1990, Umakoshi, Nakano and Yamane 1991, Kawabata, Kanai and Izumi 1985), we take the following as our input data in our computations.

(1) For the fully lamellar (FL) material,
$$\tau_{CRSS}(\text{soft mode}) = g_1^0 = 60\,\text{MPa},$$
$$\text{soft-mode hardening rate } h_{11} = 180\,\text{MPa}, \tag{10}$$
$$\tau_{CRSS}(\text{hard mode}) = g_2^0 = g_3^0 = 720\,\text{MPa},$$
$$\text{hard-mode hardening rate } h_{22} = h_{33} = 1800\,\text{MPa}.$$

(2) For NL + 4 or 12 vol% γ-TiAl;
$$\tau_{CRSS}(\text{duplex} - \gamma) = 85\,\text{MPa}, \tag{11}$$
$$\text{duplex } \gamma \text{ hardening rate, } 1500\,\text{MPa}.$$

The simulations are performed at a strain rate $1 \times 10^{-3}\,\text{s}^{-1}$, consistent with the range of testing strain rates commonly employed to generate the quasistatic experimental data; the reference shear rate $\dot{a}$ in eqn. (4) is taken as $1 \times 10^{-3}\text{s}^{-1}$. Additionally the material strain rate sensitivity exponent m is taken as 0·005, in accordance with the experimentally observed low strain rate sensitivity in the $2 \times 10^{-3}\text{s}^{-1}$ range (for example Mendiratta, Kim and Dimiduk (1993)). The elastic moduli are taken to be $\lambda = 69·7\,\text{GPa}$ and $\mu = 71·4\,\text{GPa}$ for the lamellar TiAl single crystals in our computations.

§ 3. RESULTS

In what follows, we shall show the results of numerical simulations for FL and NL (4 or 12 vol% γ-phase at the grain corners) microstructures. Comparison between available experimental evidence and our results is made, and some predictions are given. Mechanical properties such as stress–strain behaviour, localized deformation and failure modes are dealt with in detail.

3.1. *Stress–strain behaviour*

Figure 5 shows the calculated stress–strain curves for the three idealized microstructures together with the experimental data points taken from Chan and Kim (1993); the three microstructures simulated are FL, NL with 4 vol% duplex γ-phase, and NL with 12 vol% duplex γ-phase respectively. The experimental compression test was done by Chan and Kim (1993) at 25°C and at a strain rate of 0·001 s^{-1}, where the material used was Ti–47 Al–2·6 Nb–2 (Cr + V) with a NL microstructure (large lamellar grains of 1·6 mm diameter with small amount of fine grain γ grains of
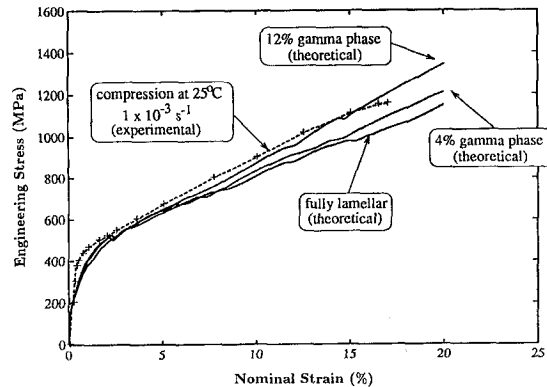
Fig. 5

Calculated stress–strain curves for the three idealized microstructures together with the experimental data points taken from Chan and Kim (1993); the three microstructures simulated are: FL, NL with 4 vol% duplex γ-phase, and NL with 12 vol% duplex γ-phase respectively.

40–50 μm diameter at colony boundaries). It is seen that good agreement is obtained between the experiment and our numerical calculations, despite a simple two-dimensional model. A slightly higher hardening rate is observed with the NL microstructure, since the strain hardening of duplex γ grains (taken as 1500 MPa) is much higher than that of the soft mode (taken as 180 MPa).

3.2. Localized deformation

3.2.1. Fully lamellar microstructure

Highly non-uniform deformation modes are developed during deformation in the FL microstructure. Figure 6 shows the accumulated sum of slips developed at various macroscopic strain levels. Highly concentrated shearing is evident at relatively small global strain levels, for example fig. 6 (a) at 2·5% global nominal strain and fig. 6 (b) at 5% global nominal strain. At higher macropscopic strain levels, that is fig. 6 (c) at 10% and fig. 6 (d) at 20% global nominal strain, deformation is still highly non-uniform. However, there are no macroscopic shear bands (MSBs) developed across the whole microstructure.

An inspection of fig. 6 shows that certain grain-boundary areas have the tendency to develop localized bands that closely aligned with a soft oriented grain's lamellar slabs (i.e. in the soft-mode slip direction) while some colonies whose lamellar slabs are almost perpendicular (i.e. $\psi \approx 90°$) have the tendency to develop 'kink bands' where these localized bands are almost perpendicular to the lamellar slabs. As examples of localized bands that are closely aligned with a soft oriented grain's lamellar slabs near the soft grain/hard grain interface boundary, we find grain 12 (soft) and grain18 (hard) in figs. 6 (a)–(d), grain 6 (soft) and grain 1 (hard) in figs. 6 (c) and (d), and grain 3 (relatively soft in terms of the local plastic deformation mode) and grain 9 (relatively hard in terms of the local plastic deformation mode) in figs 6 (c) and (d). For the case of 'kink bands', there are two types: one is close to grain boundaries, and the other is in the middle of a grain (internal buckling). Kink

Fig. 6
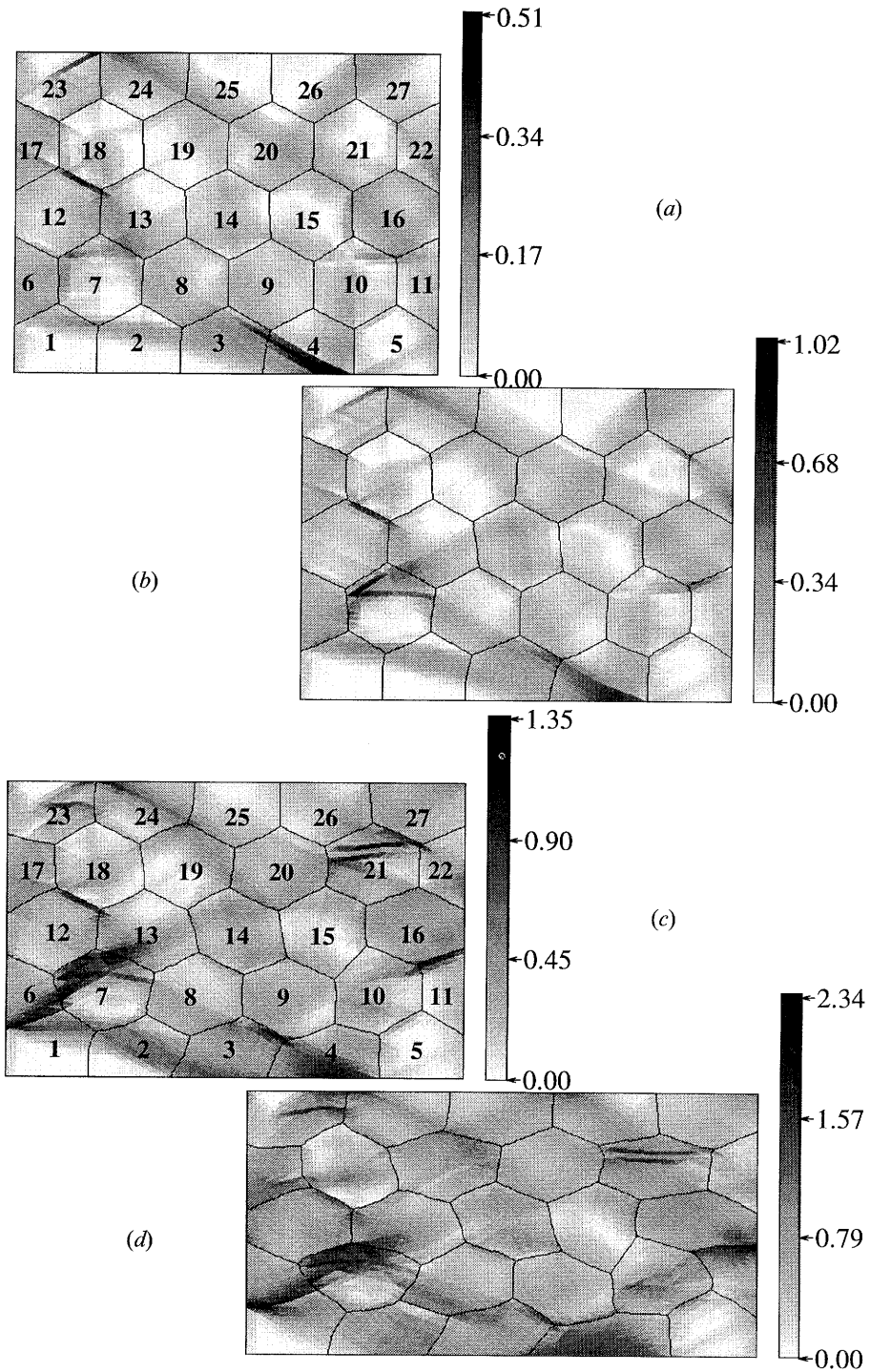
Accumulated sum of slips developed in the FL microstructure at (*a*) 2·5%, (*b*) 5%, (*c*) 10% and (*d*) 20% macroscopic strains.

bands in grain 7 near the 7–12 grain boundary (figs. 6(b) and (c)), in grain 11 near the 11–16 grain boundary (figs. 6(b) and (c)) and in grain 21 near the 21–27 grain boundary (figs. 6(b) and (c)) are examples of near-boundary 'kink bands', where the angles between the soft grain and hard grain lamellar slabs are found to be quite large (about 120–150°). Kink bands inside grain 7 and grain 21 are examples of internal buckling (see figs. 6(c) and (d)), where the initial orientations of lamellar slabs in these grains are almost parallel to the compression direction. Looking ahead to fig. 10, those 'kink bands', irrespective of whether developed near colony boundaries or within grain interiors, tend to generate very high tensile hydrostatic stresses and are therefore likely to become possible fracture initiation sites.

3.2.1. *Nearly lamellar microstructures*

Deformation modes are found to be highly non-uniform within NL microstructures as well. Figure 7 shows the accumulated sum of slips developed in the two NL microstructures (4 and 12 vol. % γ-phase) at 5% and 20% global nominal strain levels respectively. Highly concentrated shearing is evident at relatively small global strain levels, for example fig. 7(a) for 4 vol% γ-phase and for 12 vol% γ-phase (not shown) both at 5% global nominal strain. At higher macroscopic strain levels, that is fig. 7(b) for 12 vol% γ-phase and for 4 vol% γ-phase (not shown) both at

Fig. 7
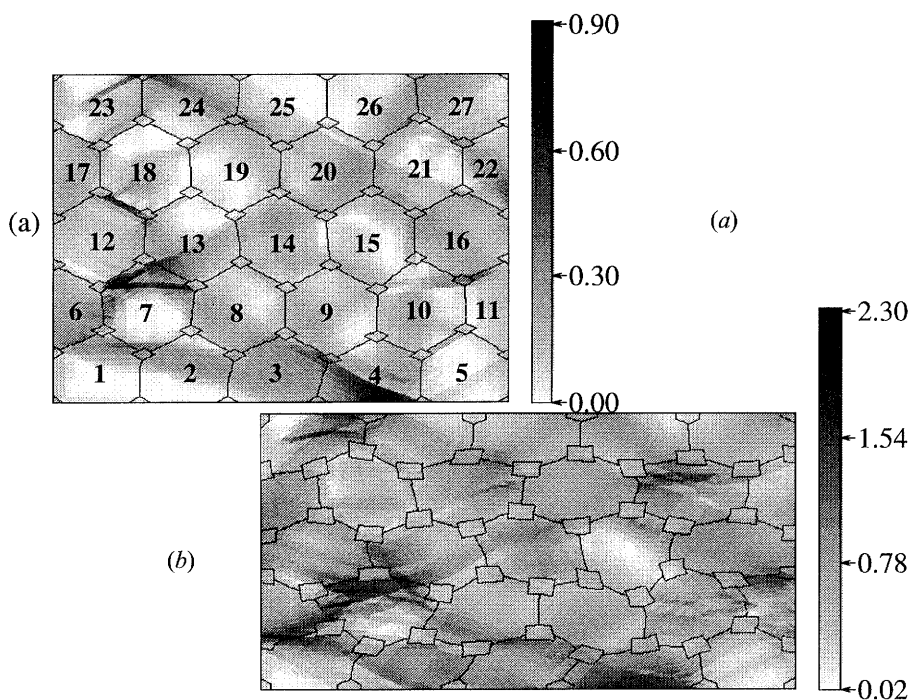
Accumulated sum of slips developed in the two NL microstructures: (a) 4 vol% γ-phase at 5% aggregate strain; (b) 12 vol% γ-phase at 20% aggregate strain.

20% global nominal strain, the deformation patterns are still highly non-uniform in the two NL microstructures. MSBs are not observed, that is no shear bands have developed across more than three grains in either of the NL microstructures, which is consistent with what is observed with the FL microstructure.

If we compare fig. 7(a) with fig. 6(b) and fig. 7(b) with fig. 6(d), localization patterns in NL microstructures are found to be very similar to that observed with the FL microstructure, that is specific sites where localized shear bands tend to form are almost the same. Bulk γ grains are more compliant (i.e. have relatively low CRSS compared with the hard-mode CRSS, and have more than five independent low-CRSS slip systems) at low strains but are quickly strain hardened owing to its significant hardening rate. Therefore localized deformation sometimes goes around the γ 'corner grains' (i.e. triple point 7–12–13 in figs. 7(a) and (b)), and no peak strain accumulations are found in those γ 'corner grains' at aggregate strains higher than 5% (see figs. 7(a) and 7(b)).

3.3. *Lattice rotation and texture development*

Lattice rotation is highly non-uniform even at low aggregate strains, which is a natural reflection of the highly non-uniform deformation within the microstructure. Figures 8(a) and (b) show contour maps of lattice rotations (in degrees) within the fully lamellar microstructure at aggregate nominal strains of 5% and 20% respec-

Fig. 8
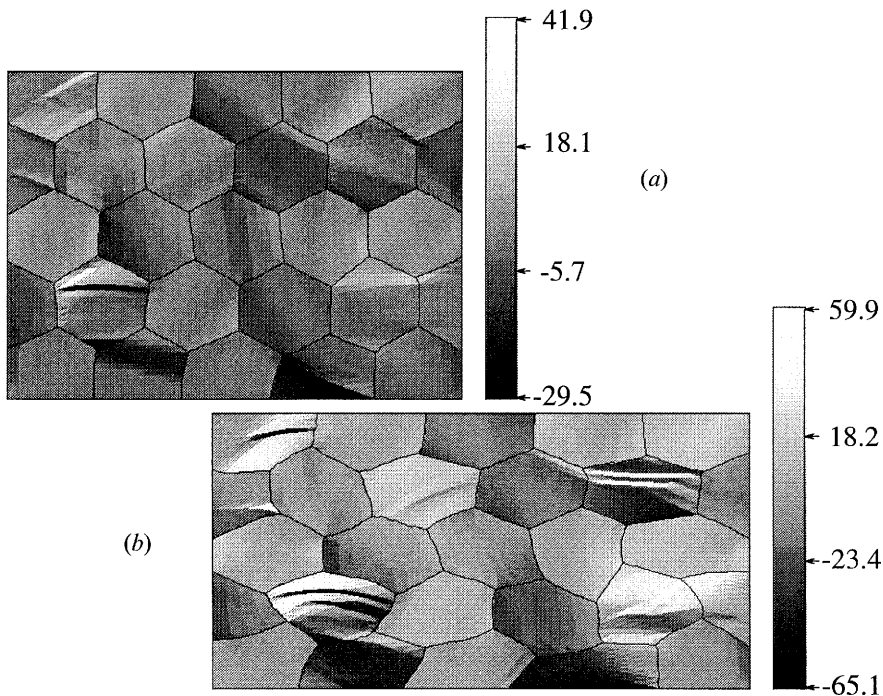
Contour maps of lattice rotation (in degrees) within the FL microstructure at aggregate nominal strains of (a) 5% and (b) 20%. Positive values show counter-clockwise rotation.

tively; positive values show counter-clockwise rotation. We can see that, at 5% aggregate strain (fig. 8 (*a*)), lattice rotations at certain regions have been as high as ± 30–$40°$. By comparing fig. 8 (*a*) with fig. 6 (*b*), and looking ahead to fig. 11 (*a*), it is evident that the non-uniform lattice rotations coincide with the localized deformations, especially with the bending and kinking of lamellar slabs. The same conclusion can be drawn at higher aggregate strains, that is 20% in fig. 8 (*b*), although peak rotations are much higher at larger strains (± 60–$65°$ in fig. 8 (*b*)). This level of magnitude of lattice rotations, inevitably, will lead to texture development of the microstructure. Note that here we deal only with textures developed during compressive deformation assuming the integrity of the microstructure (i.e. the microstructure is still a continuum solid), and no recrystallization texture effects are taken into account.

To describe texture in this two-dimensional idealized microstructure, we specify the following. The lamellar slab at each point in the microstructure (actually, in each constant strain triangle finite element) has its initial orientation $0° \leqslant \psi < 180°$ as described previously. In the deformed state, the current lamellar slab orientation ψ at each point will still be within the $0° \leqslant \psi < 180°$ range (if not, an appropriate material symmetry operation will be applied to bring it within $0° \leqslant \psi < 180°$). In order to represent this distribution of initial or deformed lamellar orientations, the interval of $0° \leqslant \psi < 180°$ is broken up into 36 subintervals: $0° \leqslant \psi < 5°, 5° \leqslant \psi < 10°, \ldots, 175° \leqslant \psi < 180°$. Associated with each of these subintervals is the volume fraction (area fraction indeed with this idealized microstructure) of the aggregate that has the lamellar orientation within the subinterval. Figures 9 (*a*) and (*b*) show the starting texture and the texture at 20% aggregate strain respectively. The starting texture in fig. 9 (*a*) is essentially random. A weak basal texture, normal to the compression axis, is developed at 20% aggregate strain (see fig. 9 (*b*)). The ideal texture orientation for this case is $\psi = 0°$ (or $180°$).

3.4. *Internal failure modes*

As noted in §§ 3.2 and 3.3, deformation in TiAl alloys is inherently non-uniform and is characterized by highly localized deformation modes. Such modes constitute

Fig. 9
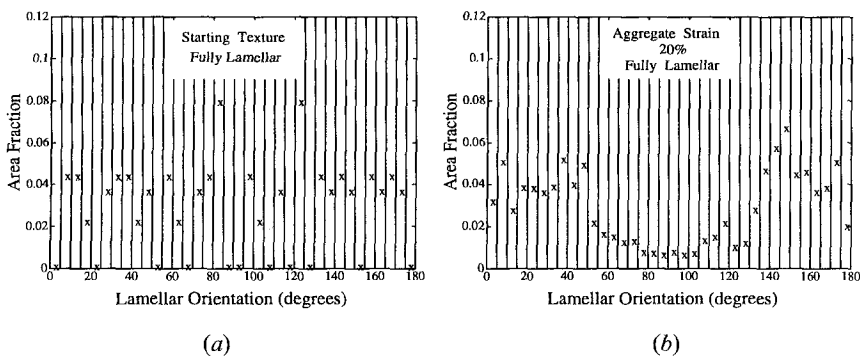
Texture development within the FL microstructure. (*a*) the starting texture, (*b*) the texture at 20% aggregate strain.

directly to failure (fracture). In what follows, it is found that in lamellar microstructures (FL and NL) under compressive loading, intergranular fracture and internal buckling (lamellar bending) are very probably two of the most important failure modes.

### 3.4.1. *Internal failure modes in the fully lamellar microstructure*

Figure 10 (*a*) shows a contour map of hydrostatic stress developed at an aggregate strain of 5%, and fig. 10 (*c*) shows the same contour map except that only stresses higher than 500 MPa are shown (pure white areas represent stresses of 500 MPa or less); fig. 10 (*b*) shows a contour map of hydrostatic stress developed at an aggregate strain of 20%, and fig. 10 (*d*) shows the same contour map except that only stresses higher than 500 MPa are shown (again, pure white areas represent stresses of 500 MPa or less).

Examine fig. 10 closely; the most striking feature is that, under *compressive* loading there are very high *tensile* hydrostatic stresses at certain sites, accompanied by high compressive hydrostatic stresses at other sites. The distribution of hydrostatic stresses is highly non-uniform (see fig. 10). At small aggregate strains, that is 5% in figs. 10 (*a*) and (*c*), high tensile hydrostatic stresses are mainly gathered near the triple points (e.g. 3–4–9, 10–11–16, 7–12–13, 12–17–18, 16–21–22 and 19–24–25 grain triple points) and grain boundaries (e.g. 3–9, 7–12, 11–16, 14–20, 20–21, 19–25 and 21–27 grain boundaries). At higher aggregate strains, that is 20% as in figs. 10 (*b*) and (*d*), high tensile hydrostatic stresses are mainly distributed within the grain interiors (grains 7, 21 and 23) in addition to the triple points (e.g. 1–2–7, 2–7–8, 8–13–14, 16–21–22 and 20–21–26 grain triple points) and grain boundaries (e.g. 3–4, 4–9, 5–10, 13–14, 13–19, 15–16 and 17–18 grain boundaries). Compare fig. 10 (*d*) with figs. 6 (*d*) and 8 (*b*); it is evident that the high tensile hydrostatic stresses within the grain interiors coincide with the internal 'kink bands' (or internal buckling) in grains 7, 21 and 23.

The very high tensile hydrostatic stress sites (greater than 1000 MPa in certain sites in our computations) are very probably the nucleation sites for fracture initiation of a debonding–decohesion type. At small strains (figs. 10 (*a*) and (*c*)), large tensile hydrostatic stresses are distributed near the grain boundaries and triple points while, at larger strains (figs. 10 (*b*) and (*d*)), internal buckling and the associated large tensile hydrostatic stresses tend to develop within grains whose lamellar slabs are nearly parallel to the loading axis in the original configuration. Therefore the results shown in fig. 10 suggest that, while fracture tends to initiate at grain boundaries and triple points at small aggregte strains, it may propagate via internal buckling (kinking) at specific sites at larger aggregate strains.
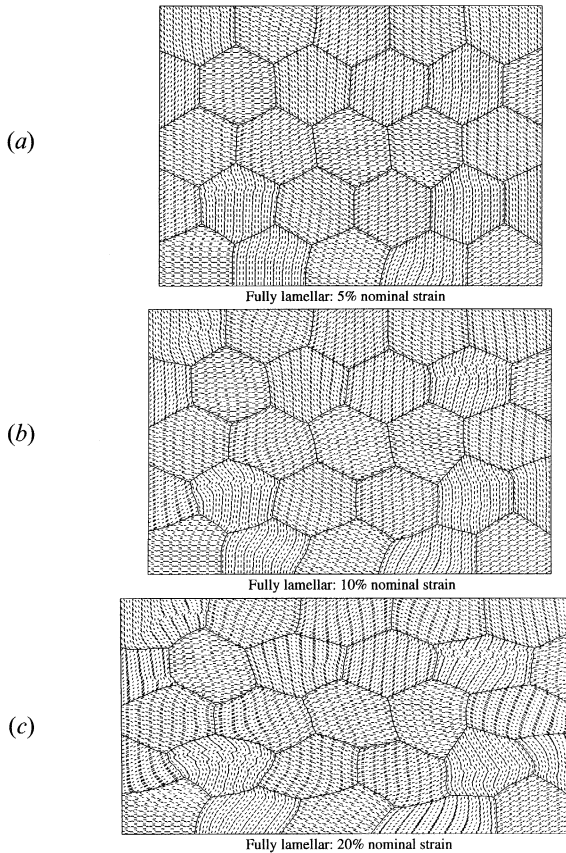
Figures 11 (*a*) (*b*) and (*c*) show the trace maps of the lamellar orientation within each finite element throughout the microstructure, at aggregate nominal strains of 5%, 10% and 20% respectively. At small aggregate strains, that is 5% in fig. 11 (*a*), although grains have not been significantly distorted, the deformation is already highly non-uniform which leads to the initiation of internal buckling (grain 7) and some general bending (grains 2, 4 and 10). The buckling or kinking is found, as expected, to happen within grains whose lamellar slabs are almost parallel to the compressive loading direction. At 10% aggregate strain (fig. 11 (*b*)), the internal buckling (or 'kink band') in grains 7, 21 and 23 is evident whereas gross lamellar bending has occured in grains 2, 4 and 10. Checking the hydrostatic stresses developed at 10% (not shown here), we find that the maximum tensile hydrostatic stresses

Ming Dao *et al.*

Fig. 10
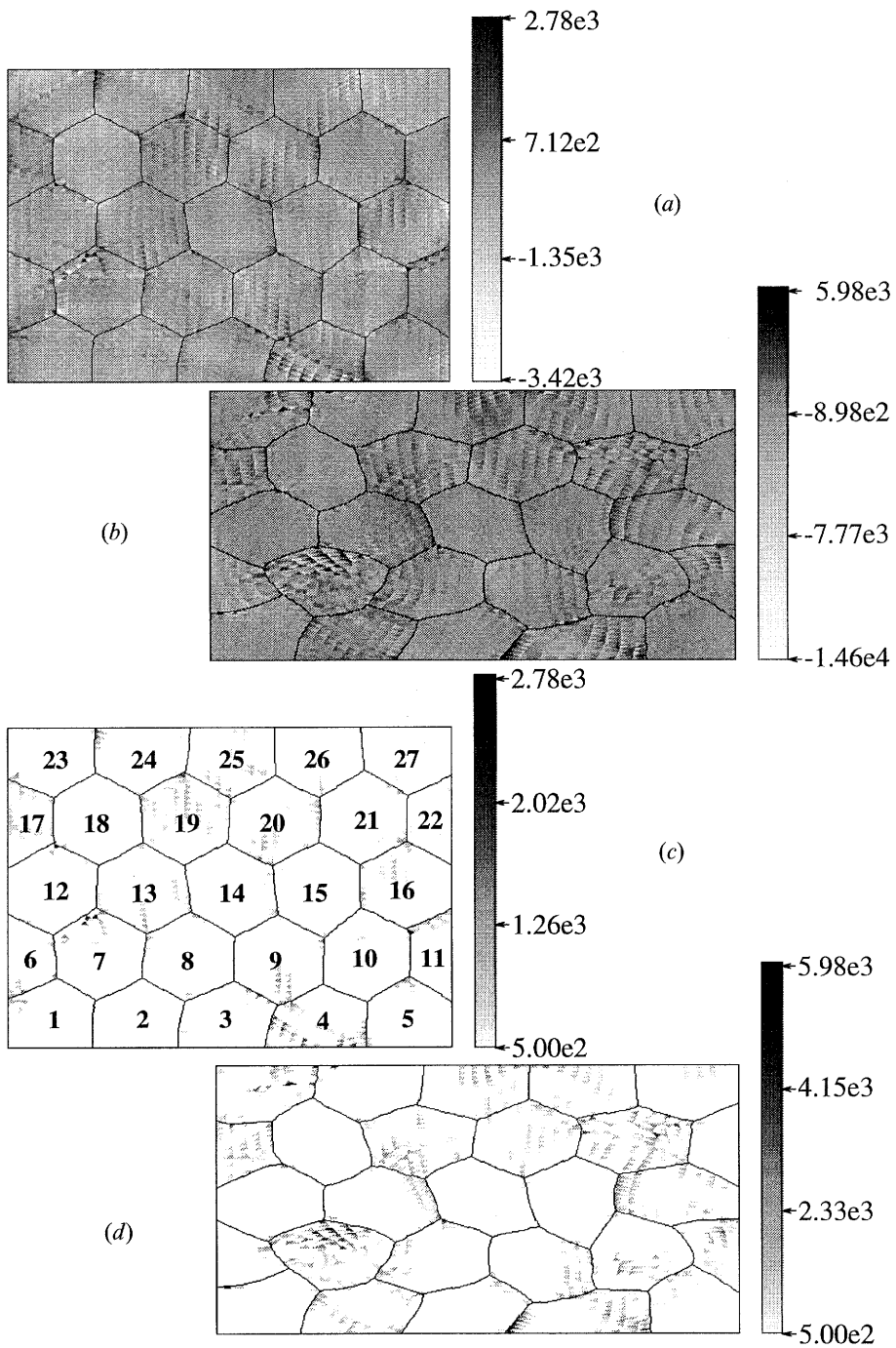
Hydrostatic stress (MPa) developed within the FL microstructure: (*a*) at an aggregate strain of 5%, (*b*) at an aggregate strain of 20%; (*c*) same as (*a*) except that only stresses higher than 500 MPa are shown; (*d*) same as (*b*) except that only stresses higher than 500 MPa are shown.

Fig. 11

Fully lamellar: 5% nominal strain

(a)

Fully lamellar: 10% nominal strain

(b)

Fully lamellar: 20% nominal strain

(c)

Trace maps of the lamellar orientation within each finite element.

have started to shift inside the buckled grains 7, 21 and 23. At 20% aggregate strain (fig. 11 (*c*)), the distortion of grains is severe, and buckling and bending are more common. At this strain level, lamellar slabs have rotated significantly from their original orientations (e.g. compare fig. 11 (*c*) with fig. 3 (*a*)).

Figure 12 (*a*) shows experimental fracture evidence of a fully lamellar polycrystalline specimen (with its external surfaces prepolished) deformed about 3% in compression at $10^{-3} \, \mathrm{s}^{-1}$ strain rate. While the bulk of the material is essentially sound, regions of microcracking and delamination are present close to the colony boundaries. Initial experiments reveal that a significant amount of microcracking precedes bulk failure and invariably has its origins at or near the grain boundary. For example, microcracks are present at strain levels of about 3%, well before the approximately 18% fracture strain in compression (Chan and Kim 1993). Since compression failures are not catastrophic, their evolution is monitored readily. Observations indicate that, at strains of the order of 10%, specific crystal orientations (lamellar nearly parallel to the loading direction) in the polycrystalline aggregates exhibit noticeable buckling behaviour (fig. 12 (*b*)).

Fig. 12
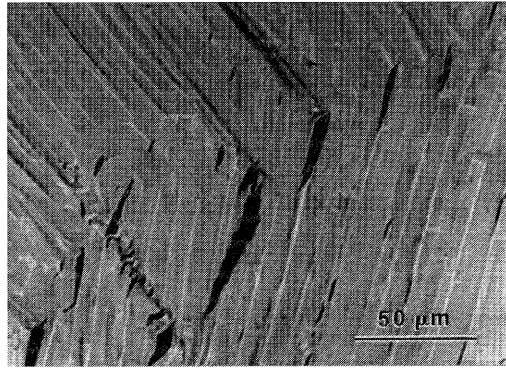
(a)
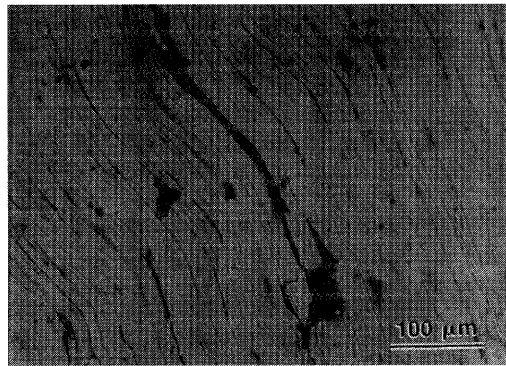
(b)

Scanning electron micrographs of two FL polycrystalline specimens (with its external surfaces
pre-polished) deformed at room temperature in compression at $10^{-3}s^{-1}$ strain rate: (a)
microcracks near a colony boundary (test stopped at a nominal strain of about 3·5%),
and (b) internal buckling (test stopped at about 15% nominal strain).

3.4.2. *Internal failure modes in nearly lamellar microstructures*

Internal failure modes in NL microstructures are very similar to those found in
FL microstructures. Similar bipolar tensile–compressive hydrostatic stress distribu-
tions are found in both NL microstructures as observed in fig. 10 for FL micro-
structure. With an examination of the hydrostatic stress developed in the NL
microstructures, one finds similar features that have developed within FL micro-
structure

(1) Under *compressive* loading, there are very high *tensile* hydrostatic stresses at
    certain sites, acccompanied by high compressive hydrostatic stresses at some
    other sites; the distribution of hydrostatic stresses is highly non-uniform.
(2) At small aggregate strains, that is about 5%, high tensile hydrostatic stresses
    are mainly gathered near the triple points and grain boundaries.
(3) At higher aggregate strains, that is 10–20%, high tensile hydrostatic stresses
    are distributed within the grain interiors in addition to the triple points and
    grain boundaries.

(4) The high tensile hydrostatic stresses developed within grain interiors at larger strains coincide with the internal 'kink bands' (or internal buckling) sites.

However, comparing the hydrostatic stress developed within NL microstructures with that developed within FL microstructure, we find that the peak hydrostatic stresses are different (looking ahead to fig. 13); at 5% strain, FL is higher than NL microstructures while, at 20% strain, NL microstructures are higher than FL microstructure.

3.4.3. *Internal failure modes against deformation and microstructure*

As discussed earlier, very high tensile hydrostatic stresses may lead to the initiation of fracture and failure. To study the development and distribution of hydrostatic stresses therefore gives us insight of how deformation and microstructure influence the failure modes.

Define 0·1 vol% averaged peak hydrostatic stress (APHS) as the hydrostatic stress averaged over the 0·1 vol% microstructure with the highest hydrostatic stresses; fig. 13 shows the 0·1 vol% APHS developed within the fully FL microstructure, the 4 vol% γ-phase NL microstructure and the 12 vol% γ-phase NL microstructure. The symbols B and I indicate whether the regions where these peak hydrostatic stresses occurred were at the grain boundaries and/or triple points or in the grain interior respectively.

As described earlier, both FL and NL microstructures have switched the peak tensile hydrostatic stress distribution, from grain boundaries and triple points, to grain interiors (coinciding with the internal buckling sites) in addition to grain boundaries and triple points. Figure 13 shows that, for the FL microstructure, the 4 vol% γ-phase NL microstructure and the 12 vol% γ-phase NL, the switch from boundaries B to interiors I are found to be at about 12.5, 10 and 10% aggregate strains respectively.

Fig. 13
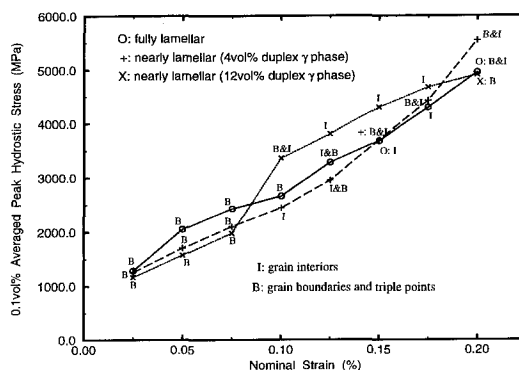
0·1 vol% APHS developed within the FL, the 4 vol% γ-phase NL and the 12 vol% γ-phase NL microstructures respectively. The symbols B and I indicate whether the regions where these peak hydrostatic stresses occurred were at the grain boundaries and/or triple points or in the grain interior respectively.

Compare the development of 0·1 vol% APHSs in 4 vol% γ-phase NL and FL microstructures in fig. 13; we notice that, at aggregate strains smaller than approximately 15%, peak hydrostatic stresses in FL are larger than that in the 4 vol% γ-phase NL microstructure and, at aggregate strains larger than approximately 15%, the peak hydrostatic stresses in the 4 vol% γ-phase NL microstructure are larger than that in the FL microstructure. If we compare the development of 0·1 vol% APHSs in the 12 vol% γ-phase NL and FL microstructures in fig. 13, a similar switch is found, except that the strain at which the switch occurs is about 7·5% instead. Noting that the γ-TiAl phase has a relatively low CRSS (taken as 85 MPa (Kawabata *et al.* 1986)) and a high hardening rate (taken as 1500 MPa), the initial compliance of γ-TiAl at the corners reduces the high tensile hydrostatic stress concentration, although the high hardening rate eventually drives the hydrostatic stress much higher after aggregate strains approximately 15% in the 4 vol% γ-phase NL microstructure and 7·5% in the 12 vol% γ-phase NL microstructure in this study. If we accept that peak tensile hydrostatic stresses can be related to failure (or fracture), then from the results presented in fig. 13 it seems that a NL microstructure containing a small volume percentage of γ-phase (i.e. 4 vol%) may lead to better ductility than the FL microstructure up to approximately 15% aggregate strain, while a NL microstructure containing a larger volume percentage of γ-phase (i.e. 12 vol%) can only yield better quasistatic fracture resistance than the FL microstructure up to about 7·5% aggregate strain. This suggests that a NL microstructure with a small volume percentage of γ-phase would have the best overall performance against fracture.

3.5. *A discussion on the influence of the intermediate mode*

From the available experimental evidence, that is fig. 1, the initial yield stresses of the intermediate mode ($\psi = 90°$) and the hard mode ($\psi = 0°$) are both much higher than that of the soft mode ($\psi \approx 45°$), which is specifically modelled in our idealized microstructure. There are some distinctive differences between the intermediate mode and the hard mode. For example, in comparison with the hard mode, the intermediate mode has a lower CRSS as well as a lower strain-hardening rate (see fig. 1). From the results shown in §§ 3.2–3.4, the localization and failure modes are found to be especially important within the intermediate-mode crystals (i.e. $\psi \approx 90°$). We thus seek to understand the influence of the intermediate mode in this section.

To identify crystals deforming via intermediate mode, a 15° cut-off range is taken, that is crystals with their original orientation within the $90° \pm 15°$ range are assumed to deform via the intermediate mode. This gives us four crystals in the idealized microstructure (see fig. 3 (*a*)), for example crystals 4, 7, 10 and 21. For these four crystals, we use lower CRSS and/or lower strain hardening values, for the 'hard-mode' slip systems ($\mathbf{s}_2, \mathbf{m}_2$) and ($\mathbf{s}_3, \mathbf{m}_3$) shown in fig. 2; the soft mode ($\mathbf{s}_1, \mathbf{m}_1$) properties are kept unchanged, although the very small Schmid factor would make it effectively inactive. Two additional calculation runs are performed, with the plastic parameters in crystals 4, 7, 10 and 21 modified for the intermediate mode. In the first calculation, only the CRSS of slip systems ($\mathbf{s}_2, \mathbf{m}_2$) and ($\mathbf{s}_3, \mathbf{m}_3$) is refined to a value that is typical for intermediate mode, where

$$\tau_{\text{CRSS}} \text{ (intermediate mode)} = g_2^0 = g_3^0 = 300 \text{ MPa}$$

is taken, with all other parameters kept the same as in eqn. (10). In the second calculation, both the CRSS and the strain hardening rate of slip systems ($\mathbf{s}_2$, $\mathbf{m}_2$) and ($\mathbf{s}_3$, $\mathbf{m}_3$) are refined to values that are typical for intermediate mode, where

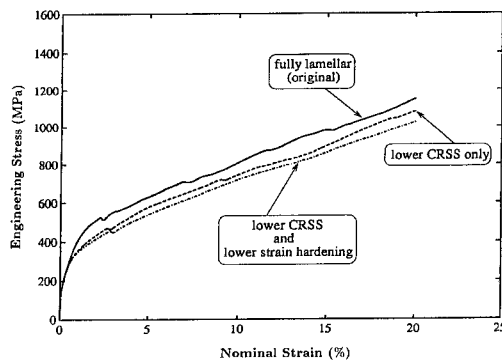$$\tau_{\text{CRSS}} \text{ (intermediate mode)} = g_2^0 = g_3^0 = 300 \, \text{MPa},$$

$$\text{intermediate-mode hardening rate } h_{22} = h_{33} = 180 \, \text{MPa},$$

are taken, with all other parameters kept the same as in eqn. (10).

Figure 14 shows the two calculated stress–strain curves together with the original FL curve. The stress–strain curves, calculated using lower CRSS or lower CRSS plus lower strain-hardening rates, are a little softer as expected. However, the differences between the three curves are found to be small. Figure 15 shows the lamellar slab traces at 15% aggregate strain using original FL parameters, lower CRSS refined for intermediate mode, and lower CRSS plus lower strain-hardening rate refined for intermediate mode respectively. Internal buckling modes are present in all three calculations. It is clear that, with both the CRSS and the strain hardening refined for the intermediate mode, the internal buckling of 'kinking' is much less intense than that computed from the original FL parameters while, with only the CRSS refined for the intermediate mode, there is no significant change within the buckled crystals.
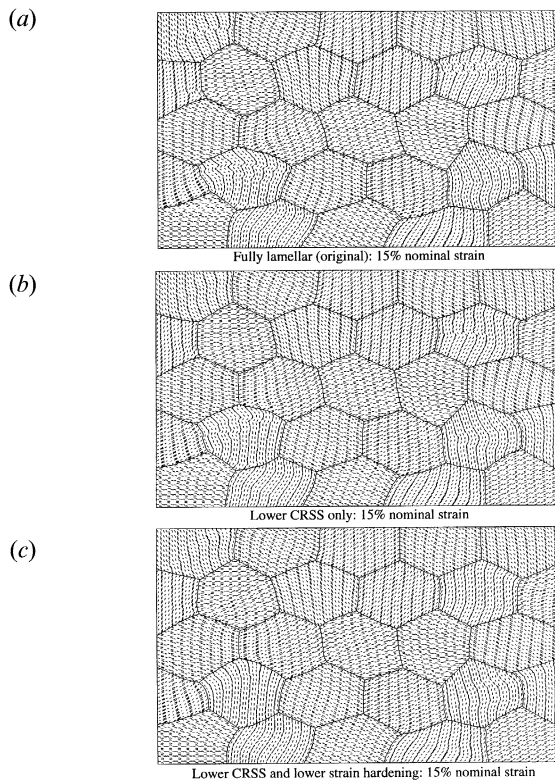
From the texture evolution shown in fig. 9, we note that, at 20% aggregate strain, only about 3 vol% of the microstructure are within the $90 \pm 15°$ intermediate-mode window. This shows that, as the deformation gets larger, the initially intermediate-mode-oriented grains will rotate away from the angle $\psi = 90°$. Therefore the real material response is better modelled by both the CRSS and the strain-hardening rate refined for intermediate mode at small strains (i.e. strains less than 5–10%), while at large strains (i.e. strains larger than 10%) the original soft-mode and hard-mode parameters work better.

Fig. 14

Effects of the intermediate mode on the stress–strain behaviour.

Fig. 15

(*a*)

Fully lamellar (original): 15% nominal strain

(*b*)

Lower CRSS only: 15% nominal strain

(*c*)

Lower CRSS and lower strain hardening: 15% nominal strain

Lamellar slab traces at 15% aggregate strain using different parameters for intermediate mode

§ 4. CONCLUSION

A physically based micromechanical model is developed to study finite compressive deformation and failure modes in polycrystalline FL and NL TiAl microstructures. Strong orientation-dependent yield behaviour of lamellar TiAl single crystals is specifically modelled, while polycrystalline stress–strain behaviour, localized deformation, lattice rotation and texture development, and failure modes are studied using large-scale finite-element calculations. For FL and NL TiAl microstructures under compressive loading, we conclude the following.

(1) Deformation and lattice rotations within the microstructure are found highly non-uniform, as suggested by our earlier results (Kad, Dao and Asaro 1995a, Dao, Kad and Asaro 1995). There is also a weak basal texture, normal to the compression axis, developing at only 20% aggregate strain.

(2) At small strains, that is about 5% aggregate strain, intergranular fracture is the likely major fracture initiation mode, consistent with our previous results.

(3) At larger strains, that is starting from 5–10% aggregate strain, fracture initiated by internal buckling should be increasingly important. Internal buckling is found in lamellar TiAl crystals whose lamellae are initially nearly parallel to the compressive loading.

(4) Small amounts of equiaxed γ grains at the boundaries and triple points can reduce the tensile hydrostatic stress concentration. However, there exists an optimal γ volume fraction that gives the best overall performance *vis-à-vis* flow strength against the crack initiating peak tensile hydrostatic stresses.

REFERENCES

ASARO, R. J., 1979 *Acta metall.*, **27**, 445.
ASARO, R. J., and RICE, J. R., 1977, *J. Mech. Phys. Solids*, **25**, 309.
CHAN, K. S., and KIM, Y.-W., 1993, *Metall. Trans.* A, **24**, 113.
DAO, M., and ASARO, R. J., 1993, *Mater. Sci. Engng* A, **170**, 143.
DAO, M., KAD, B. K., and ASARO, R. J., 1995, *High Temperature Ordered Intermetallic Alloys VI*, Materials Research Society Symposium Proceedings, Vol. 364, edited by J. A. Horton, I. Baker, S. Hanada R. D. Noebe and D. S. Schwartz (Pittsburgh, Pennsylvania: Materials Research Society), pp. 1029–1034.
DAVIDSON, D. L., and CAMPBELL, J. B., 1993, *Metall Trans.* A, **24**, 1555.
FUJIWARA, T., NAKAMURA, A. M., HOSOMI, M., NISHITANI, S. R., SHIRAI, Y., and YAMAGUCHI, M., 1990, *Phil. Mag*, A, **61**, 591.
HARREN, S. V., and ASARO, R. J., 1989, *J. Mech. Phys. Solids*, **37**, 191.
HARREN, S. V., DÈVE, H. E., and ASARO, R. J., 1988, *Acta metall*, **36**, 2435.
HILL, R., 1963, *J. Mech. Phys. Solids*, **10**, 1.
HILL, R., and RICE, J. R., 1972, *J. Mech. Phys. Solids*, **20**, 401.
INUI, H., OH, M H., NAKAMURA, A., and YAMAGUCHI, M., 1992, *Acta metall.*, **40**, 3095.
KAD, B. K., DAO, M., and ASARO, R. J., 1995a, *Phil Mag.* A, **71**, 567; 1995b, *Mater Sci. Engng* A, **193**, 97; 1995c, *High Temperature Ordered Intermetallic Alloys VI*, Materials Research Society Symposium Proceedings, Vol. 364, edited by J. A. Horton, I. Baker, S. Hanada, R. D. Noebe and D. S. Schwartz (Pittsburgh, Pennsylvania: Materials Research Society), pp. 169–174.
KAWABATA, T., KANAI, T., and IZUMI, O., 1985, *Acta metall.*, **33**, 1355.
KIM, Y.-W., 1991, *High-Temperature Ordered Intermetallic Alloys IV*, Materials Research Society Symposium Proceedings, Vol. 213, edited by L. A. Johnson, D. P. Pope and J. O. Stiegler (Pittsburgh, Pennsylvania: Materials Research Society), pp. 777–794.
McHUGH, P. E., ASARO, R. J., and SHIH, C. F., 1993, *Acta metall.*, **41**, 1461.
MENDIRATTA, M. G., KIM, Y.-W., and DIMIDUK, D. M., 1993, *High-Temperature Ordered Intermetallic Alloys V*, Materials Research Society Symposium Proceedings, Vol. 288, edited by I. Baker, R. Darolia, J. D. Whittenberger and M. H. Yoo (Pittsburgh, Pennsylvania: Materials Research Society), pp. 543–548.
PIERCE, D., ASARO, R. J., and NEEDLEMAN, A., 1983, *Acta metall.*, **31**, 1951.
UMAKOSHI, Y., NAKANO, T., and YAMANE, T., 1991, *Scripta metall.*, **25**, 1525.